Ab initio study of multiferroic $BiFeO_3$ (110) surfaces

Takahiro Shimada,[1,*] Kou Arisue,[1] Jie Wang,[1,2] and Takayuki Kitamura[1]

[1]*Department of Mechanical Engineering and Science, Kyoto University, Nishikyo-ku, Kyoto 615-8540, Japan*

[2]*Department of Engineering Mechanics, School of Aeronautics and Astronautics, Zhejiang University, Hangzhou 310027, China*

(Received 20 January 2014; revised manuscript received 22 May 2014; published 23 June 2014)

The nature of multiferroic surfaces, more specifically, the energetic, ferroelectric, and noncollinear magnetic properties of $BiFeO_3$ (110) surfaces, is investigated using *ab initio* (first-principles) calculations based on the fully unconstrained spin-density functional theory. As in the case of other perovskite oxides, the O-terminated surface is found to be energetically favorable. The spontaneous polarization and magnetic moment at the surface rotate in different ways from their counterparts in the bulk, which leads to a unique magnetoelectric response at the surface. The detailed lattice-distortion-mode (symmetry) analysis reveals that the rotation of the ferroelectric polarization results from the additional symmetry breaking due to the surface termination, whereas the rotation of the magnetic moment is predominantly caused by the magnetocrystalline anisotropy. Furthermore, we investigate the effect of epitaxial strain and find that the strain responses of both the polarization and the magnetic moment are markedly enhanced at the surfaces.

DOI: 10.1103/PhysRevB.89.245437 PACS number(s): 75.85.+t, 68.35.−p, 31.15.A−

I. INTRODUCTION

Bismuth ferrite ($BiFeO_3$) is one of the most important classes of perovskite oxides because of its ferroelectric and simultaneously coexisting ferromagnetic/antiferromagnetic orderings at room temperature, i.e., multiferroics [1]. These two ferroic orderings not only coexist in the material, but also strongly couple with each other: The coupling effect is known as magnetoelectric coupling, which enables spontaneous magnetization (polarization) to be controlled by applying an external electric (magnetic) field [2]. Owing to its intriguing properties, multiferroic $BiFeO_3$ has the potential to be used in next-generation devices, such as multistate memory elements, transducers, sensors, and spintronics devices [1,3–5]. All these applications are realized in complex components or thin-film geometries. A recent dramatic advance in fabrication technology enables us to obtain ultrathin films with extremely small dimensions, down to several nanometers in thickness [6,7]. Since the surface-to-volume ratio of such ultrathin films is extremely high, surface effects can dominate. Thus, the multiferroic properties in the vicinity of such surfaces have been drawing immense interest.

The rapid change in coordination number at $BiFeO_3$ surfaces can significantly affect the multiferroic properties: Since ferroelectricity is a complex phenomenon resulting from the delicate balance between long-range Coulomb and short-range covalent interactions [8,9], unique ferroelectric properties tend to arise where these interactions are locally cut by the surface terminations on the $BiFeO_3$ surfaces and the delicate balance is perturbed. On the other hand, the magnetism, carried by the directional *d* orbitals of the body-centered Fe, is sensitive to the crystal field of the surrounding oxygen octahedra [10]. The presence of surfaces leads to breaking of the crystal field, which in turn alters local magnetic moments as well as the magnetocrystalline anisotropy. In addition, the variety of structural distortions (symmetries) observed in perovskite oxides accounts for their intriguingly rich properties [11]. Indeed, the Γ_4^- mode, one of the major structural distortions in $BiFeO_3$, is responsible for ferroelectricity, whereas another distortion of the R_4^+ mode induces a small canting of the magnetic moment of Fe atoms, resulting in weak ferromagnetism in the $BiFeO_3$ system [12]. Here, the symmetry breaking of surface terminations introduces additional structural distortions to the $BiFeO_3$ lattice, which would result in a novel ferroic ordering. Thus, the $BiFeO_3$ surface is expected to possess unique multiferroic properties, distinctive from those of the bulk. However, the intrinsic multiferroic properties of $BiFeO_3$ surfaces have yet to be thoroughly investigated.

In addition, multiferroic thin films, which are normally fabricated on a substrate by epitaxial growth [13–15], are typically subjected to mechanical strains due to the lattice mismatch between the thin films and the substrate. Since the ferroelectric and magnetic properties of $BiFeO_3$ are sensitive to mechanical strains [16–19], it is worth investigating the effect of epitaxial strain.

Theoretical calculations based on the density functional theory [20,21] (DFT) and the DFT plus on-site Hubbard *U* (DFT + *U*) method [22] have successfully reproduced the structural, ferroelectric, and magnetic ground states of $BiFeO_3$ [23] and have provided a comprehensive insight into ferroelectric and magnetic properties in connection with the structural distortions and/or symmetries in $BiFeO_3$ [24]. In the present study, we perform *ab initio* (first-principles) calculations using the DFT + *U* method to investigate the intrinsic ferroelectric and magnetic properties of $BiFeO_3$ (110) surfaces in which the ferroelectric polar axis of $[1\bar{1}1]$ is parallel to the surface. The $BiFeO_3$ (110) surfaces are thus free from any surface charges and concomitant depolarizing fields, which enables us to determine the intrinsic properties of the surface structure itself. We also carry out the computations applying epitaxial strain in order to clarify the strain response of the ferroelectric and magnetic properties of $BiFeO_3$ surfaces. Through this study, one of the complexities and novelties included in the $BiFeO_3$ nanostructures can be theoretically identified. This factor is the ideal one which is free from many other factors, such as defects and impurities, but it has the potential to give

*Email address: shimada@me.kyoto-u.ac.jp

a valuable suggestion for some experimentally observed rich multiferroic properties of $BiFeO_3$.

II. COMPUTATIONAL DETAILS

A. Simulation method

Ab initio (first-principles) calculations based on the density functional theory with a plane-wave basis set are performed using the Vienna *ab initio* simulation package [20,21]. The cutoff energy of the plane waves is 500 eV. The electron-ion interaction is described by the projector augmented wave potentials [25,26], which explicitly include the Bi $5d$, $6s$, and $6p$, the Fe $3p$, $3d$, and $4s$, and the O $2s$ and $2p$ electrons in the valence states. A $2 \times 3 \times 1$ Monkhorst-Pack [27] k-point mesh is used for Brillouin-zone integrations. To treat the exchange-correlation energy, we use the local spin-density approximation plus U method [22] with the values $U = 3.3$ and $J = 0.8$ eV. We perform noncollinear magnetic calculations with fully unconstrained formalism [28], which explicitly include spin-orbit coupling (SOC) [29] to describe spin canting and the resulting weak ferromagnetism in $BiFeO_3$, as well as the magnetocrystalline anisotropy of the surface.

B. Simulation models and procedure

Figure 1(a) shows the unit cell of bulk rhombohedral ($R3c$) $BiFeO_3$. Mainly two types of structural distortions are found in the $BiFeO_3$ lattice: (i) ferroelectric (FE) distortions associated with an irreducible representation of Γ_4^- and (ii) antiferrodistortive rotations of O_6 octahedra corresponding to the R_4^+ mode. The FE distortions of bulk $BiFeO_3$ are in the $[1\bar{1}1]$ direction in the figure, resulting in a spontaneous polarization **P** in the same direction. The magnetic moments are essentially in the rock-salt antiferromagnetic (AFM) (G-type AFM) order but with a small spin canting due to the R_4^+ mode [12]. The canting of the magnetic moments results in a macroscopic magnetization $\boldsymbol{M}_{\rm tot}$ in the $[1\bar{1}\,\bar{2}]$ direction.

Figure 1(b) shows the atomic structures of $BiFeO_3$ (110) surfaces with three possible terminations. The $BiFeO_3$ (110) surfaces are *nonstoichiometric* (O, FeO, and Bi terminations) with a zigzag shape, which were found to be more energetically favorable than the *stoichiometric* (110) surfaces (O_2 and BiFeO terminations) with a flat shape in many perovskite oxides [30–32]. The simulation model for the O-terminated (110) surface of $BiFeO_3$ is depicted in Fig. 1(c). The x, y, and z axes in the Cartesian setting are along the [001], $[1\bar{1}0]$, and [110] directions, respectively. The film is 23 atomic layers in thickness, which is thick enough to avoid the interaction between the upper and the lower surfaces. Since a three-dimensional periodic boundary condition is applied in the calculations, a vacuum region of $l_v = 16$ Å is introduced in the z direction so that undesirable interactions from neighboring films are sufficiently avoided. Thus, the simulation cell dimensions in the x, y, and z directions are given by $2a$, $\sqrt{2}a$, and $5.5\sqrt{2}a + l_v$, where a, the lattice constant of bulk rhombohedral ($R3c$) $BiFeO_3$, is 3.90 Å.

To obtain the equilibrated structure of the models, the atomic positions are fully relaxed using the conjugate-gradient method until all the Hellmann-Feynman forces are less than 5.0×10^{-2} eV/Å. To further investigate the effect of epitaxial (misfit) strains, a small increment of strain $\Delta\varepsilon_{\rm ep}$ ($=\Delta\varepsilon_{xx} = \Delta\varepsilon_{yy}$) is applied stepwise along both the x and the y directions. At each strain step, atoms are again fully relaxed by the same above-mentioned procedure.

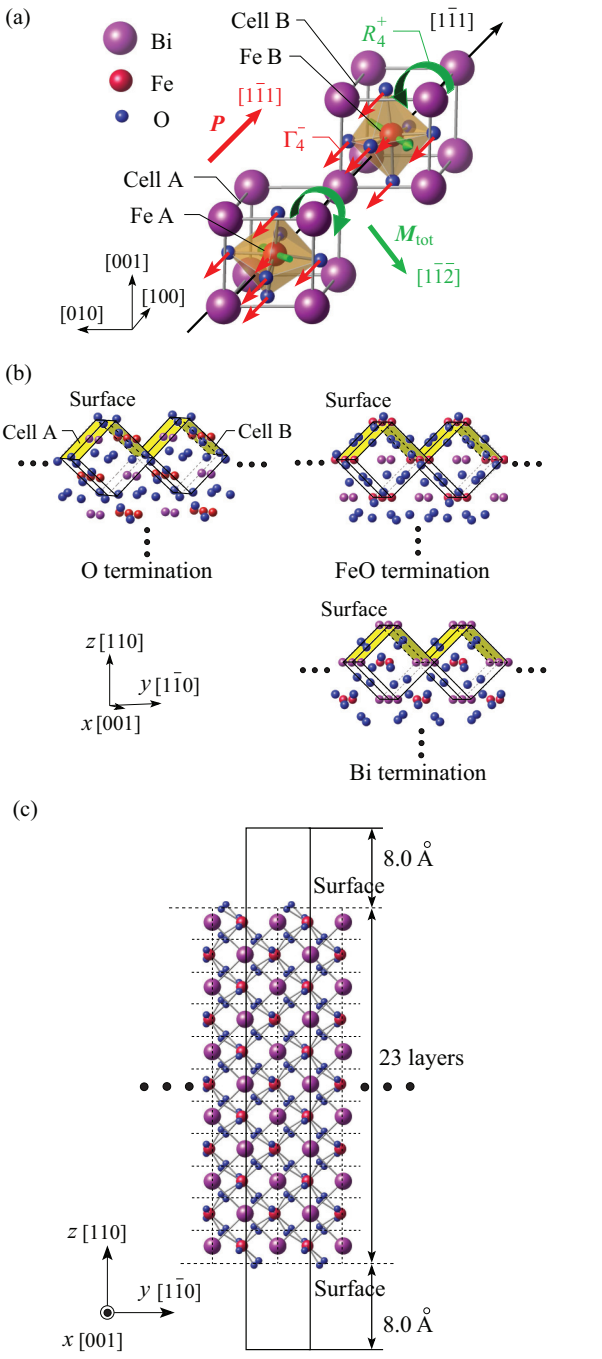

FIG. 1. (Color online) (a) Crystal structure of bulk rhombohedral ($R3c$) $BiFeO_3$. The green arrows that penetrate into the Fe atoms indicate the magnetic moments. (b) Side view of the three *nonstoichiometric* (110) surfaces (O, FeO, and Bi terminations) of $BiFeO_3$. (c) Simulation model for the O-terminated (110) surface. The solid box represents the simulation supercell.

TABLE I. Calculated surface energies E_{surf}, cleavage energies E_{surf}^{cleav}, and relaxation energies E_{rel} (in J/m^2) of $BiFeO_3$ (110) surfaces with O, FeO, and Bi terminations.

Termination	O	FeO	Bi
E_{surf}^{cleav}	1.82	2.64	2.64
E_{rel}	− 0.61	− 1.17	− 0.73
E_{surf}	1.21	1.47	1.91

III. RESULTS AND DISCUSSIONS

A. Surface energies and stability of (110) surfaces

To investigate the stability of surfaces in $BiFeO_3$, we introduce the surface energy parameter E_{surf}, defined as the energy needed to make new surfaces from the bulk. The surfaces analyzed in the present paper are *nonstoichiometric*, so we use the following expression for the surface energy, formulated by Eglitis and Rohlfing [31] and Eglitis and Vanderbilt [32],

$$E_{surf}(X) = E_{surf}^{cleav}(X) + E_{rel}(X), \tag{1}$$

where X denotes O-, FeO-, or Bi-terminated surfaces, $E_{surf}^{cleav}(X)$ is the cleavage energy of the unrelaxed surface, and $E_{rel}(X)$ is the (negative) surface relaxation energy. The cleavage of $BiFeO_3$ slabs at the O_2 layer results in the formation of two equivalent O-terminated surfaces, whereas Bi- and its complementary FeO-terminated surfaces are formed at the BiFeO layer. Thus, the cleavage energy of the unrelaxed $BiFeO_3$ (110) surface is

$$E_{surf}^{cleav}(\mathrm{O}) = \frac{1}{2S}\left[E_{slab}^{unr}(\mathrm{O}) - 11E_{bulk}\right], \tag{2}$$

$$E_{surf}^{cleav}(\mathrm{FeO}) = \frac{1}{4S}\left[E_{slab}^{unr}(\mathrm{Bi}) + E_{slab}^{unr}(\mathrm{FeO}) - 22E_{bulk}\right], \tag{3}$$

or

$$E_{surf}^{cleav}(\mathrm{Bi}) = \frac{1}{4S}\left[E_{slab}^{unr}(\mathrm{Bi}) + E_{slab}^{unr}(\mathrm{FeO}) - 22E_{bulk}\right], \tag{4}$$

where S is the surface area, $E_{slab}^{unr}(X)$ (X = O−, FeO-, or Bi-terminated surface) are the total energies of the unrelaxed slabs, and E_{bulk} is the total energy per bulk unit cell with ten atoms. The surface relaxation energy is

$$E_{rel}(X) = \frac{1}{2S}\left[E_{slab}^{rel}(X) - E_{slab}^{unr}(X)\right], \tag{5}$$

where $E_{slab}^{rel}(X)$ is the total slab energy after relaxation.

The calculated surface energies E_{surf}, cleavage energies E_{surf}^{cleav}, and relaxation energies E_{rel} of $BiFeO_3$ (110) surfaces with O, FeO, and Bi terminations are listed in Table I. Among all the surfaces, the O-terminated (110) surface has the lowest surface energy (1.21 J/m^2), the FeO-terminated surface has the second lowest (1.47 J/m^2), and the surface energy with Bi termination is relatively high (1.91 J/m^2). These results show that the O-terminated surface is the most stable, the FeO-terminated surface is the second most stable, and the Bi-terminated surface is the most unlikely surface among the (110) surfaces.

The main reason why the O-terminated surface is the most stable is because its cleavage energy (1.82 J/m^2) is much lower than that of the FeO- or Bi-terminated surface (2.64 J/m^2). The difference in stability between the FeO- and the Bi-terminated surfaces is due to the fact that the relaxation energies differ depending on the type of termination: The relaxation energy of a surface with FeO termination (−1.17 J/m^2) is lower than that of a surface with Bi termination (−0.73 J/m^2), which suggests that the former changes more markedly during relaxation.

In a previous paper [32], similar analyses for (110) surfaces of other perovskite oxides were performed, and the surface energies were found to be about 1 to 2 J/m^2. In another *ab initio* calculation [33] involving $SrTiO_3$, $BaTiO_3$, $CaTiO_3$, and $BaZrO_3$ (110) surfaces, the O-terminated (110) surface always exhibited the lowest surface energy. These results corroborate our calculations.

Note that the surface energy in our calculation is only an indication of the surface stability in vacuum, and it gives us no information as to which surface termination is the most stable under particular environmental conditions. In order to resolve this issue, the surface grand potential [34,35] would be useful. It should be addressed in a future paper.

B. Ferroelectric and magnetic properties at surfaces

In order to determine the ferroelectricity at $BiFeO_3$ surfaces, we introduce the site-by-site local polarization **P**, which can be evaluated via

$$\mathbf{P} = \frac{e}{\Omega_c}\sum_j w_j \int_0^{\mathbf{u}_j^*} \mathbf{Z}_j^* d\mathbf{u}_j, \tag{6}$$

where Ω_c, e, and $\mathbf{u}_j^*$ denote the unit-cell volume, the electron charge, and the atomic displacement vector from the ideal lattice site of atom j, respectively. The index j covers all atoms in the unit cell. The weights (w) are set separately according to the terminations: 1/2 for Bi, 1/4 for Fe, and 1/2 or 1/8 for O for the O termination, 1 for Bi, 1/8 for Fe, and 1/4 for O for the FeO termination, 1/8 for Bi, 1 for Fe, and 1/2 for O for the Bi termination. These correspond to the number of unit cells that share the atom. $\mathbf{Z}_j^*$ is the Born effective charge tensor of bulk $BiFeO_3$, which is dependent on the atomic displacements. In the case of $PbTiO_3$, the $\mathbf{Z}_j^*$ dependence on the displacements is weak enough for $\mathbf{Z}_j^*$ to be regarded as a constant. Then, Eq. (6) can be approximated by

$$\mathbf{P} = \frac{e}{\Omega_c}\sum_j w_j \mathbf{Z}_j^* \mathbf{u}_j^*, \tag{7}$$

where $\mathbf{Z}_j^*$ of the undistorted or distorted structure alone is applied. For $BiFeO_3$, however, Eq. (7) does not yield an accurate result: 121.0 μC/cm^2 for $\mathbf{Z}_j^*$ of the undistorted (cubic: $Pm\bar{3}m$) structure, and 64.7 μC/cm^2 for $\mathbf{Z}_j^*$ of the distorted (rhombohedral: $R3c$) structure of bulk $BiFeO_3$ because the $\mathbf{Z}_j^*$ dependence on the displacements in $BiFeO_3$ is relatively large (see Table II). Thus, we have to use Eq. (6), which is the original definition of polarization. However, this is computationally costly because we have to calculate quite so many $\mathbf{Z}_j^*$'s of each state from an undistorted to a distorted structure. We then assume that $\mathbf{Z}_j^*$ varies linearly with $\mathbf{u}_j$,

$$\mathbf{Z}_j^* = \mathbf{A}_j \mathbf{u}_j + \mathbf{B}_j, \tag{8}$$

TABLE II. The local polarization in bulk $BiFeO_3$ calculated using Born effective charges of the cubic ($Pm\bar{3}m$) phase, rhombohedral ($R3c$) phase, and the *linear* method. The exact polarization value is also determined using Berry phase theory.

	$Pm\bar{3}m$	$R3c$	*Linear* interpolation	Berry phase
$\|\mathbf{P}\|$ (μC/cm^2)	121.0	64.7	92.8	91.7

where $\mathbf{A}_j$ and $\mathbf{B}_j$ are constant tensors that can be determined by the $\mathbf{Z}_j^*$ of both the undistorted $Pm\bar{3}m$ and the distorted $R3c$ phases. Then, the local polarization $\mathbf{P}$ becomes

$$\mathbf{P} = \frac{e}{\Omega_c} \sum_j w_j \int_0^{\mathbf{u}_j^*} (\mathbf{A}_j \mathbf{u}_j + \mathbf{B}_j) du_j. \quad (9)$$

When we use this *linear* interpolation, the local polarization of bulk $BiFeO_3$ can be calculated to be $|\mathbf{P}| = 92.8$ μC/cm^2. This is in good agreement with the 91.7 μC/cm^2 determined by the Berry phase theory [36].

Table III and Fig. 2 show the $\mathbf{P}$ for $BiFeO_3$ (110) surfaces and its visualization, respectively. The surface layer consists of two unit cells, labeled cell A and cell B. Thus, the values of $\mathbf{P}$ for each unit cell are also listed in Table III. For the bulk, $\mathbf{P}$ lies purely on the x-y plane parallel to the (110) surface, and the out of plane P_z is zero (the direction of $\mathbf{P}$ is then $[1\bar{1}1]$). In addition, the $\mathbf{P}$'s in cells A and B are exactly the same. For the O-terminated surface, the in plane P_x and P_y are smaller than those for the bulk, and the out of plane P_z is nonzero. These findings suggest that the polarization vector rotates in a different direction at the surface than in the bulk (see also Fig. 2). The rotational angle θ of $\mathbf{P}$ from the bulk is 11.7°, and its direction is almost $[8\bar{5}5]$. Moreover, each component of $\mathbf{P}$ in cells A and B is slightly different from each other. This suggests that an antiferroelectric (AFE) state emerges in addition to the FE state at the surface. A rotation of the polarization at the surface can also be seen in the FeO and Bi terminations, but the amplitude and direction of the rotation depends on the termination type: $\theta = 4.3°$ for the FeO termination (direction:

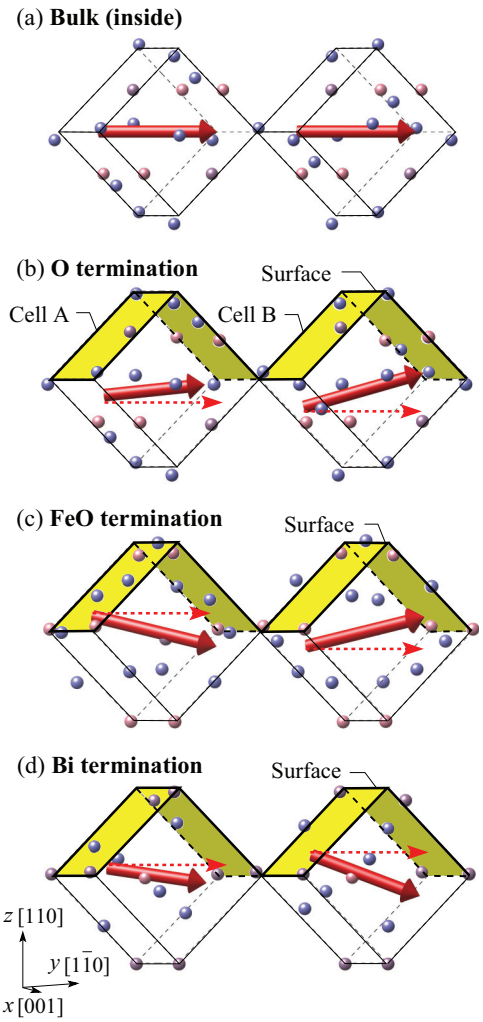

FIG. 2. (Color online) The local polarization vectors $\mathbf{P}$ for (a) the bulk and the surface with (b) O termination, (c) FeO termination, and (d) Bi termination. The dashed red arrows in (b)–(d) represent the polarization vectors for the bulk.

TABLE III. Each component of the polarization $\mathbf{P}$ for the bulk and the $BiFeO_3$ (110) surfaces with O, FeO, and Bi terminations, the rotational angle θ of $\mathbf{P}$ from the bulk, and the direction of $\mathbf{P}$. Since the surface layer consists of two unit cells, cells A and B, the local polarization in each unit cell is also listed. The x, y, and z directions correspond to [001], [1$\bar{1}$0], and [110], respectively.

		P_x (μC/cm^2)	P_y (μC/cm^2)	P_z (μC/cm^2)	θ (deg)	Direction
Bulk (inside)	Cell A	53.1	75.4	0.0		$[1\bar{1}1]$
	Cell B	53.1	75.4	0.0		$[1\bar{1}1]$
	Total	53.1	75.4	0.0		$[1\bar{1}1]$
O termination	Cell A	35.5	56.2	4.8	5.1	$[6\bar{5}5]$
	Cell B	43.6	74.8	24.8	16.7	$[8\bar{4}5]$
	Total	39.6	65.5	14.8	11.7	$[8\bar{5}5]$
FeO termination	Cell A	56.2	72.9	− 21.5	13.4	$[2\bar{4}3]$
	Cell B	59.6	67.0	20.7	14.5	$[2\bar{1}1]$
	Total	57.9	70.0	− 0.4	4.3	$[6\bar{6}7]$
Bi termination	Cell A	42.8	71.8	− 6.2	6.2	$[4\bar{5}4]$
	Cell B	56.3	77.3	− 31.6	18.3	$[4\bar{9}7]$
	Total	49.6	74.6	− 18.9	12.0	$[4\bar{7}5]$

TABLE IV. Each componentof the magnetic moment $\boldsymbol{M}$ for the bulk and the $BiFeO_3$ (110) surfaces with O, FeO, and Bi terminations, the canting angle φ of $\boldsymbol{M}_{Fe}$ from the ideal G-type AFM, and the direction of the total magnetic moment $\boldsymbol{M}_{tot}$. The x, y, and z directions correspond to [001], [1$\bar{1}$0], and [110], respectively.

		M_x (μB/Fe)	M_y (μB/Fe)	M_z (μB/Fe)	φ (deg)	Direction
Bulk (inside)	Fe A	− 0.055	0.039	3.89	1.0	
	Fe B	− 0.055	0.039	− 3.89	1.0	
	Total	− 0.055	0.039	0		[1$\bar{1}$2]
O termination	Fe A	− 0.210	− 0.238	3.81	4.8	
	Fe B	0.042	0.237	− 3.77	3.7	
	Total	− 0.084	− 0.001	0.02		[11$\bar{6}$]
FeO termination	Fe A	− 0.037	− 0.066	3.72	1.2	
	Fe B	− 0.018	0.046	− 2.80	1.0	
	Total	− 0.028	− 0.010	0.46		[110]
Bi termination	Fe A	− 0.244	− 0.132	3.89	4.1	
	Fe B	0.114	0.194	− 3.89	3.3	
	Total	− 0.065	0.031	0.00		[11$\bar{3}$]

[6$\bar{6}$7]) and $\theta = 12.0^\circ$ for the Bi termination (direction: [4$\bar{7}$5]). The difference in the polarization of cells A and B (and the resulting AFE state) is also observed in the case of the FeO and Bi terminations. These surface effects gradually decrease with increasing distance from the surface, and starting with eight to nine layers beneath the surface, they disappear for all the surfaces. As a whole, the magnitude of spontaneous polarization tends to decrease at the (110) surfaces because of the low coordination number and the appearance of an AFE state. This theoretical result could correspond to experimental observations that the spontaneous polarization of (110) $BiFeO_3$ thin films is smaller than those of bulk and (111) thin films, suggesting that the (110) surfaces of thin films may reduce the observed spontaneous polarizations [37,38]. Note that the effects of surface charges and the resulting depolarizing field at $BiFeO_3$ (110) surfaces are quite low due to the small canting of polarization. In contrast, $BiFeO_3$ thin films with (001) or (111) surfaces are expected to possess much larger surface charges. This may lead to the significant suppression of polarization or the emergence of ferroelectric polydomains. This issue may be left for future papers.

Table IV and Fig. 3 show the magnetic moment $\boldsymbol{M}$ for $BiFeO_3$ (110) surfaces and its visualization, respectively. The surface layer contains two Fe atoms, Fe A and B. Thus, the local magnetic moment $\boldsymbol{M}_{Fe}$ of each Fe atom and the total magnetic moment $\boldsymbol{M}_{tot}$ of the two Fe atoms are listed. For the bulk, $\boldsymbol{M}_{Fe}$ lies almost along the out of plane z direction and has a small value for the in plane M_x and M_y owing to spin canting (canting angle φ: 1.0°). The total magnetic moment $\boldsymbol{M}_{tot}$ of the two Fe atoms is on the x-y plane and its direction is [1$\bar{1}$ $\bar{2}$]. For the O-terminated surface, the in plane M_x and M_y of the local magnetic moments are several times larger than those for the bulk. This indicates that the spin canting of $\boldsymbol{M}_{Fe}$ is much larger at the surface than in the bulk: The canting angles φ for $\boldsymbol{M}_{Fe}$ of Fe A and B are 4.8° and 3.7°, respectively (see also Fig. 3). Due to the enhancement in the canting of $\boldsymbol{M}_{Fe}$ at the surface, the direction of the total magnetic moment $\boldsymbol{M}_{tot}$ changes to [11$\bar{6}$]. A similar trend can be seen in the case of the Bi-terminated surface. The canting of $\boldsymbol{M}_{Fe}$ is considerably enhanced at the surface compared to the bulk, resulting in a

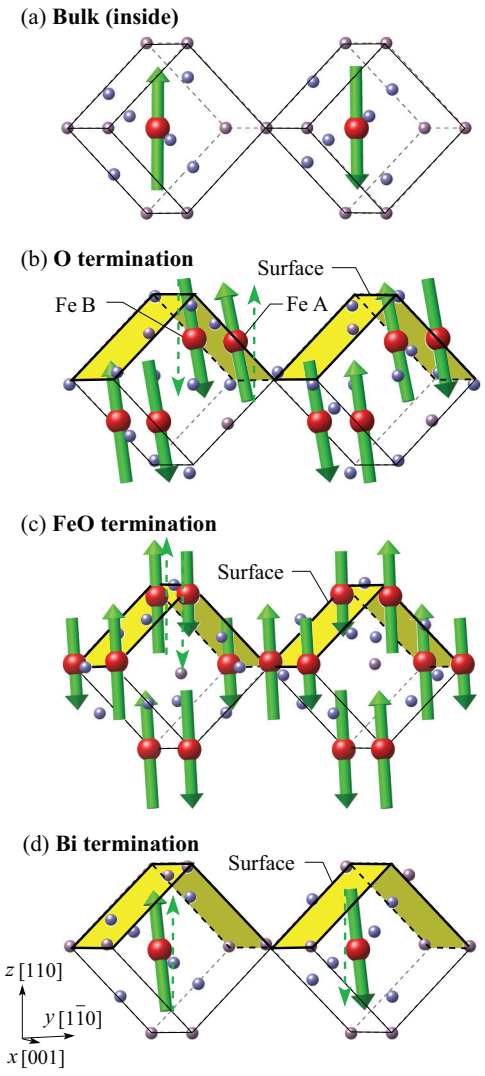

FIG. 3. (Color online) (a) The local magnetic moment vectors $\boldsymbol{M}_{Fe}$ for (a) the bulk and the surface with (b) O termination, (c) FeO termination, and (d) Bi termination. The dashed green arrows in (b)–(d) represent the magnetic-moment vectors for the bulk.

TABLE V. The structural distortion modes observed for O-, FeO-, and Bi-terminated (110) $BiFeO_3$ surfaces. The components of Γ_4^- and R_4^+ represent the amplitude in the (x, y, z) directions, which correspond to [001], $[1\bar{1}0]$, and [110], respectively.

	Γ_4^-(FE) (Å)	R_4^+(AFD) (Å)	Additional distortions
Bulk (inside)	(0.14,0.19,0.00)	(0.28,0.40,0.00)	
			X_1^+(AFE)
			X_5^+(AFE)
O termination	(0.12,0.09,0.03)	(0.25,0.44,−0.06)	
			X_1^+(AFE)
FeO termination	(0.19,0.13,−0.01)	(0.31,0.15,0.02)	X_5^+(AFE)
			R_5^+(AFE)
			X_3^-(AFE)
Bi termination	(0.13,0.19,−0.05)	(0.31,0.48,0.01)	X_5^-(AFE)
			R_4^-(AFE)
			M_5^-(FE)

different $\boldsymbol{M}_{\text{tot}}$ direction. For the FeO-terminated surface, φ is the same as in the bulk, but $\boldsymbol{M}_{\text{tot}}$ is much larger compared to the other terminations. These surface effects on the magnetic moments diminish as the distance from the surface increases, disappearing about 11 layers beneath the surface. Thus, the magnitude of total magnetic moment at the (110) surfaces tends to increase due to rotation of the local spin moment of Fe. This theoretical result also corresponds to experimental facts that the observed magnetic moment tends to increase as the size of the $BiFeO_3$ nanoparticles decreases (i.e., the surface area with respect to the volume increases and thereby, the effect of the surface becomes dominant [39]).

To summarize, $BiFeO_3$ (110) surfaces cause the polarization and magnetic moment to rotate in ways different from those in the bulk, depending on the type of termination. This can lead to the distinct anisotropies in the magnetoelectric response.

C. Structural distortion modes at the surfaces

Table V shows the structural distortion modes observed in the $BiFeO_3$ (110) surfaces. The mode analysis was performed using the software ISODISPLACE [40]. For the rhombohedral $BiFeO_3$ bulk, the perovskite lattice exhibits only two types of structural distortions, namely, the ferroelectric Γ_4^- mode and the antiferrodistortive R_4^+ mode as shown in Fig. 1(a). The amplitudes of the Γ_4^- and R_4^+ modes represent the sum of the distortions of all three atoms and the distortion of oxygen, respectively. For the O-terminated surface, the amplitude of each component of Γ_4^- is different from the bulk due to symmetry breaking at the surface. The in plane x and y components of Γ_4^- are smaller than those in the bulk. The out of plane z component, on the other hand, has a positive value at the surface, whereas there is no z component in the bulk. These clearly correspond to the behavior of polarization at the surface. Thus, the rotation of polarization at the surface is primarily caused by the change in the Γ_4^- mode due to the symmetry breaking at the surface. A similar trend is observed in FeO- and Bi-terminated surfaces: The amplitudes of Γ_4^- roughly correspond to the polarizations at the surfaces. Moreover, symmetry breaking at the surface generates several additional distortion modes, which can affect the ferroelectricity. These additional distortion modes are not dominant factors (the amplitudes are about 10%–30% of the Γ_4^- mode) but have a significant effect on the surface ferroelectricity. The X_1^+ and X_5^+ modes are the two main modes generated in the case of the O-terminated surface. These two modes show opposite displacement directions in cells A and B (see Fig. 4), resulting in the AFE state described in the previous section. Additional distortion modes that induce AFE patterns can also be seen at FeO- and Bi-terminated surfaces, but the types of modes are different from those of the O-terminated surface. This indicates that the symmetry-breaking pattern depends on the type of termination, leading to a variety of polarization distributions at surfaces.

In the bulk, the R_4^+ mode induces the canting of the local magnetic moment and a concomitant weak ferromagnetism.

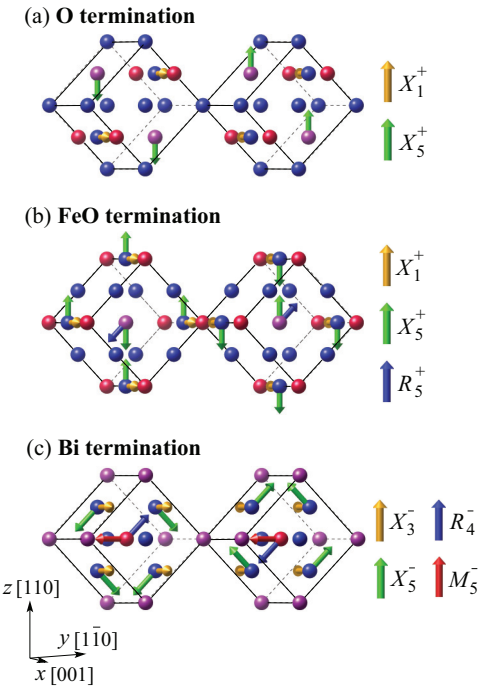

FIG. 4. (Color online) Schematic of the additional distortion modes for (a) O-terminated, (b) FeO-terminated, and (c) Bi-terminated surfaces.

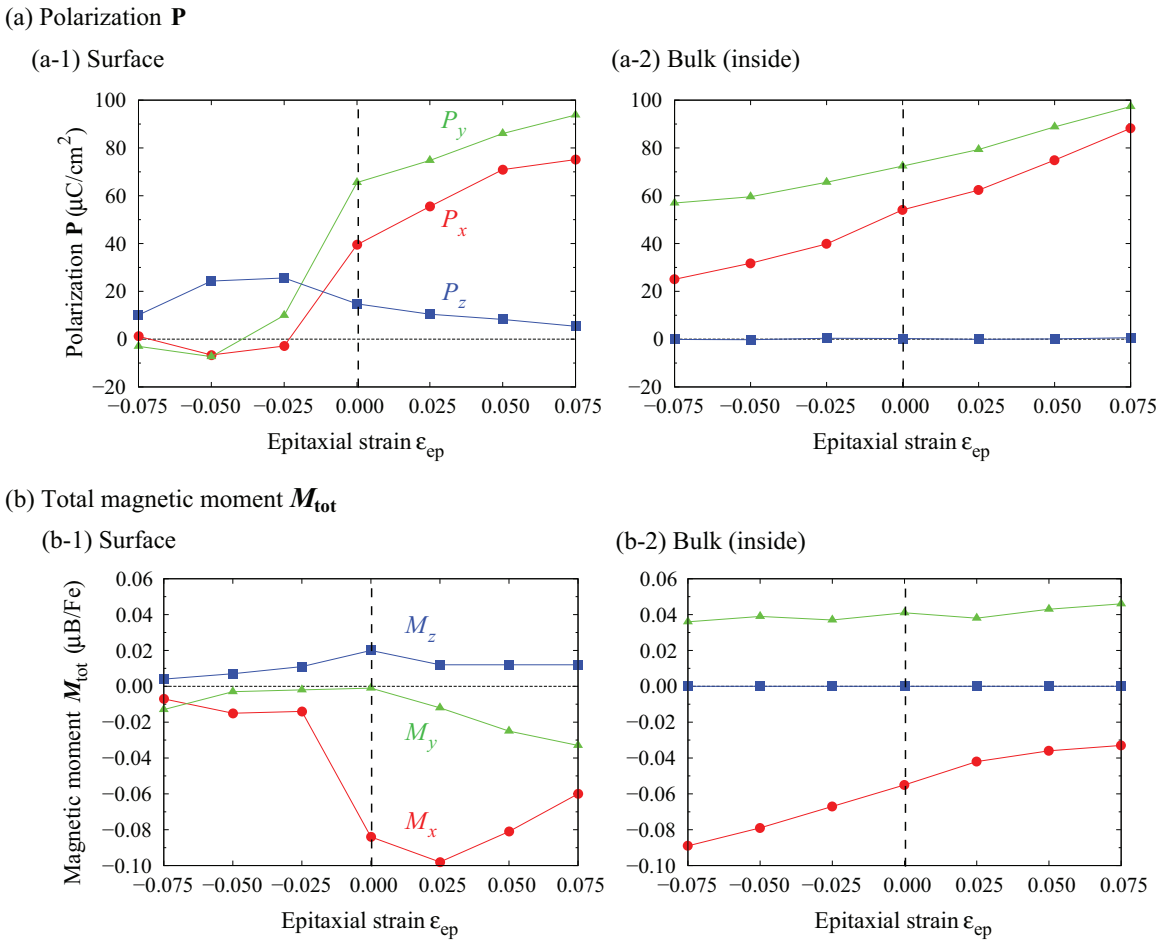

FIG. 5. (Color online) (a) Polarization **P** and (b) total magnetic moment $\boldsymbol{M}_{tot}$ as a function of epitaxial strain ε_{ep} for a $BiFeO_3$ (110) surface with the O termination. **P** and $\boldsymbol{M}_{tot}$ for the bulk are also shown for comparison. The x, y, and z directions correspond to [001], $[1\bar{1}0]$, and [110], respectively.

The canting angle φ is roughly proportional to the amplitude of R_4^+. Compared to the bulk, φ is 3.7–4.8 times larger for the O-terminated surface, whereas the amplitudes of R_4^+ are not that different from each other. Therefore, the markedly enhanced spin canting at the surface cannot be explained by the change in R_4^+ alone. We believe that the main cause of the large spin canting at the surface might be the magnetocrystalline anisotropy. Magnetocrystalline anisotropy is related to crystal symmetry, which determines the unique easy axis of the magnetic moment in the bulk. At surfaces, the magnetocrystalline anisotropy affects the magnetic moment differently, owing to the symmetry breaking and the resulting structural anisotropy, which may lead to a distinct rotation of the magnetic moment. Indeed, we additionally performed the noncollinear DFT calculations of the O-terminated surface with different magnetic orientations from what we obtained in the precious section (its direction is [110]). The magnetic orderings of these states are energetically equivalent in the bulk because their magnetic moments are on the same $(1\bar{1}1)$ easy plane, i.e., [011] and $[10\bar{1}]$ directions, but these are not the same as [110] at the (110) surfaces due to the symmetry breaking. By taking the energy difference between the two magnetic states of [110] and $[011]/[10\bar{1}]$ directions, we have obtained the magnetocrystalline anisotropy energy by 0.16 meV/Fe, although it is completely zero in the bulk. This clearly shows that the magnetocrystalline anisotropy is largely enhanced at the surface. Furthermore, another noncollinear DFT calculation *without* SOC results in no spin canting, i.e., almost no effect from the surface. Since inclusion of the SOC effect induces magnetocrystalline anisotropy, canting of the magnetic moment at the surface is predominated by magnetocrystalline anisotropy.

D. Strain effect on ferroelectric and magnetic properties at the surface

Finally, we briefly discuss the influence of epitaxial strain on the polarization and magnetic moment at the most favorable O-terminated surface. Figure 5(a) shows the polarization **P** at the surface and in the bulk as a function of epitaxial strain ε_{ep}. In the bulk, **P** increases (decreases) gradually under increasing tensile (compressive) strain. In contrast, for the O-terminated surface, the response of the polarization to the strain differs markedly between the cases of tensile and compressive strains. Under compressive strain, **P** decreases sharply, dropping to almost zero, whereas under tensile strain, it gradually increases as in the bulk. For all of the strain points, we again performed the mode analysis. As a result, it has been revealed that the

change in the Γ_4^- mode at the surface with respect to the strain corresponds well to the behavior of the surface polarization. This shows that the Γ_4^- mode mainly determines the surface polarization even under the effect of strain. Figure 5(b) plots the total magnetic moment $\boldsymbol{M}_{\rm tot}$ at the surface and in the bulk as a function of $\varepsilon_{\rm ep}$. For the bulk, each component of $\boldsymbol{M}_{\rm tot}$ changes continuously with the epitaxial strain, leading to a small decrease (increase) in $\boldsymbol{M}_{\rm tot}$ as a result of the tension (compression). For the O-terminated surface, on the other hand, $\boldsymbol{M}_{\rm tot}$ falls rapidly, reaching zero under compressive strain, whereas it changes continuously under tensile strain. The mode analysis has revealed that the behavior of the R_4^+ mode at the surface with respect to the strain does not correspond to the surface magnetization. For example, the R_4^+ mode at $\varepsilon_{\rm ep} = -0.025$ is not so much different from that at $\varepsilon_{\rm ep} = +0.000$, although $\boldsymbol{M}_{\rm tot}$ rapidly drops to 0. This indicates that the R_4^+ mode is not the dominant factor for the surface magnetization even under the strain, but magnetocrystalline anisotropy predominates. In conclusion, the strain responses of $\mathbf{P}$ and $\boldsymbol{M}_{\rm tot}$ are markedly enhanced at the surface, especially under compressive strain.

IV. CONCLUSION

In this study, the ferroelectric and magnetic properties of $BiFeO_3$ (110) surfaces with three possible *nonstoichiometric* terminations (O, FeO, and Bi) were investigated using *ab initio* (first-principles) DFT + U calculations. We have identified the O-terminated surface to be most likely to appear on the basis of energy cost of surface formation, i.e., surface energy. At the surfaces, both the polarization and the magnetic moment rotate in different ways from in the bulk, and these rotational characteristics strongly depend on the type of termination. Such local rotations induce a distinctly anisotropic magnetoelectric coupling at the $BiFeO_3$ surface. The surface effects continue as far as about 11 layers (approximately 15 Å) beneath the surface. The detailed lattice distortion mode analysis has further revealed that the change in the structural distortion modes due to the symmetry breaking at the surface determines the rotation of the polarization. The rotation of the magnetic moment at the surface, on the other hand, is predominantly governed by the magnetocrystalline anisotropy. We simultaneously carried out a strain analysis and found that the strain responses of the polarization and the magnetic moment are markedly enhanced at the surface.

ACKNOWLEDGMENTS

The authors acknowledge financial support for T.S. and T.K. from a Grant-in-Aid for Specially Promoted Research (Grant No. 25000012) from the Japan Society for the Promotion of Science (JSPS) and for J.W. from the Nature Science Foundation of China (Grants No. 11321202 and No. 11090333), Zhejiang Provincial Natural Science Foundation (Grant No. R6110115), and Postdoctoral Fellowship For Foreign Researchers (Grant No. P12058) from JSPS.

[1] G. Catalan and J. F. Scott, Adv. Mater. **21**, 2463 (2009).
[2] H. Ohno, Science **281**, 951 (1998).
[3] M. Fiebig, T. Lottermoser, D. Fröhlich, A. V. Goltsev, and R. V. Pisarev, Nature (London) **419**, 818 (2002).
[4] N. A. Spaldin and M. Fiebig, Science **309**, 391 (2005).
[5] J. F. Scott, Nature Mater. **6**, 256 (2007).
[6] M. Gajek, M. Bibes, S. Fusil, K. Bouzehouane, J. Fontcuberta, A. Barthélémy, and A. Fert, Nature Mater. **6**, 296 (2007).
[7] Y. H. Chu, T. Zhao, M. P. Cruz, Q. Zhan, P. L. Yang, L. W. Martin, M. Huijben, C. H. Yang, F. Zavaliche, H. Zheng, and R. Ramesh, Appl. Phys. Lett. **90**, 252906 (2007).
[8] R. Resta, M. Posternak, and A. Baldereschi, Phys. Rev. Lett. **70**, 1010 (1993).
[9] W. Zhong, R. D. King-Smith, and D. Vanderbilt, Phys. Rev. Lett. **72**, 3618 (1994).
[10] J. M. Rondinelli and N. A. Spaldin, Adv. Mater. **23**, 3363 (2011).
[11] P. S. Halasyamani and K. R. Poeppelmeier, Chem. Mater. **10**, 2753 (1998).
[12] C. Ederer and N. A. Spaldin, Phys. Rev. B **71**, 060401 (2005).
[13] D. Ricinschi, K. Y. Yun, and M. Okuyama, J. Phys.: Condens. Matter **18**, L97 (2006).
[14] J. Seidel, L. W. Martin, Q. He, Q. Zhan, Y.-H. Chu, A. Rother, M. E. Hawkridge, P. Maksymovych, P. Yu, M. Gajek, N. Balke, S. V. Kalinin, S. Gemming, F. Wang, G. Catalan, J. F. Scott, N. A. Spaldin, J. Orenstein, and R. Ramesh, Nature Mater. **8**, 229 (2009).
[15] J. H. Lee, L. Fang, E. Vlahos, X. Ke, Y. W. Jung, L. F. Kourkoutis, J.-W. Kim, P. J. Ryan, T. Heeg, M. Roeckerath, V. Goian, M. Bernhagen, R. Uecker, P. C. Hammel, K. M. Rabe, S. Kamba, J. Schubert, J. W. Freeland, D. A. Muller, C. J. Fennie, P. Schiffer, V. Gopalan, E. Johnston-Halperin, and D. G. Schlom, Nature (London) **466**, 954 (2010).
[16] C. Ederer and N. A. Spaldin, Phys. Rev. B **71**, 224103 (2005).
[17] O. E. González-Vázquez and J. Íñiguez, Phys. Rev. B **79**, 064102 (2009).
[18] J. C. Wojdeł and J. Íñiguez, Phys. Rev. Lett. **105**, 037208 (2010).
[19] T. Shimada, K. Arisue, and T. Kitamura, Phys. Lett. A **376**, 3368 (2012).
[20] G. Kresse and J. Hafner, Phys. Rev. B **47**, 558 (1993).
[21] G. Kresse and J. Furthmüller, Phys. Rev. B **54**, 11169 (1996).
[22] V. I. Anisimov, F. Aryasetiawan, and A. I. Liechtenstein, J. Phys.: Condens. Matter **9**, 767 (1997).
[23] J. B. Neaton, C. Ederer, U. V. Waghmare, N. A. Spaldin, and K. M. Rabe, Phys. Rev. B **71**, 014113 (2005).
[24] O. Diéguez, O. E. González-Vázquez, J. C. Wojdeł, and J. Íñiguez, Phys. Rev. B **83**, 094105 (2011).
[25] P. E. Blöchl, Phys. Rev. B **50**, 17953 (1994).
[26] G. Kresse and J. Joubert, Phys. Rev. B **59**, 1758 (1999).
[27] H. J. Monkhorst and J. D. Pack, Phys. Rev. B **13**, 5188 (1976).
[28] D. Hobbs, G. Kresse, and J. Hafner, Phys. Rev. B **62**, 11556 (2000).

[29] O. Grotheer, C. Ederer, and M. Fähnle, Phys. Rev. B **63**, 100401 (2001).
[30] G. X. Zhang, Y. Xie, H. T. Yu, and H. G. Fu, J. Comput. Chem. **30**, 1785 (2009).
[31] R. I. Eglitis and M. Rohlfing, J. Phys.: Condens. Matter **22**, 415901 (2010).
[32] R. I. Eglitis and D. Vanderbilt, Phys. Rev. B **76**, 155439 (2007).
[33] R. I. Eglitis, Integr. Ferroelectr. **108**, 11 (2007).
[34] X.-G. Wang, A. Chaka, and M. Scheffler, Phys. Rev. Lett. **84**, 3650 (2000).
[35] A. Pojani, F. Finocchi, and C. Noguera, Surf. Sci. **442**, 179 (1999).
[36] R. Resta, J. Phys.: Condens. Matter **12**, R107 (2000).
[37] W. Ratcliff, II, D. Kan, W. Chen, S. Watson, S. Chi, R. Erwin, G. J. Mclntyre, S. C. Capelli, and I. Takeuchi, Adv. Funct. Mater. **21**, 1567 (2011).
[38] S. K. Lee, B. H. Choi, and D. Hesse, Appl. Phys. Lett. **102**, 242906 (2013).
[39] H. Yang, T. Xian, Z. Q. Wei, J. F. Dai, J. L. Jiang, and W. J. Feng, J. Sol-Gel Sci. Technol. **58**, 238 (2011).
[40] B. J. Campbell, H. T. Stokes, D. E. Tanner, and D. M. Hatch, J. Appl. Crystallogr. **39**, 607 (2006).